Crustal Storage and Ascent Rates of the Mt. Shasta Primitive Magnesian Andesite

by

Mitchell Phillips

A Thesis Presented in Partial Fulfillment
of the Requirements for the Degree
Master of Science

Approved November 2019 by the
Graduate Supervisory Committee:

Christy Till, Chair
Richard Hervig
Melanie Barboni

ARIZONA STATE UNIVERSITY

December 2019

ABSTRACT

Primitive arc magmas provide a critical glimpse into the geochemical evolution of subduction zone magmas, as they represent the most unadulterated mantle-derived magmas observed in nature in these tectonic environments and are the precursors of the more abundant andesites and dacites typical in arcs. To date, the study of primitive arc magmas has largely focused on their origins at depth, while significantly less is known about pre-eruptive crustal storage and ascent history. This study examines the crustal storage and ascent history of the Mt. Shasta primitive magnesian andesite (PMA), the demonstrated dominant parent magma for the abundant mixed andesites erupted at Mt. Shasta. Petrographic and geochemical observations of the PMA identify a mid-crustal magma mixing event with a less evolved relative of the PMA recorded in multiple populations of reversely zoned clinopyroxene and orthopyroxene phenocrysts. Prior phase equilibrium experiments and thermobarometric calculations as part of this study suggest the PMA experienced storage, mixing with a less evolved version of itself, and subsequent crystallization at 5kbar and 975°C. Modeling of Fe-Mg interdiffusion between the rims and cores of the reversely-zoned clinopyroxene and orthopyroxenes suggest this mixing, crystallization and subsequent ascent occurred within 10 years, or ~$2.9^{+6.5}_{-2.5}$ years, prior to eruption. Ascent from 5kbar or ~15 km, with no meaningful shallower storage, suggests minimum crustal transit rates of ~5 km/year. This rate is comparable to only a couple of other similar types of crustal transit rates (and slower than the much faster, syn-eruptive ascent rates measured through methods like olivine-hosted melt embayment volatile gradients and U-series isotope measurements on other arc magmas). The results of this study help to constrain the pre-eruptive history and ascent

rates of hydrous primitive arc magmas, illuminating their magmatic processes during ascent. When combined with geophysical signals of magma movement, mixing to eruption timescales such as this have the power to inform volcanic hazard models for monogenetic, cinder cone eruptions in the Southern Cascades.

DEDICATION

For the fam: Susan, Greg, Emma, Maggie, and Remy

ACKNOWLEDGMENTS

This research was supported by the NSF CAREER Grant awarded the C. B. Till: Triggering Eruptions: Determination of P-T-x-t Histories for Magmatic Bodies Preceding Eruption EAR 1654584. Special thanks to Axel Wittman for assistance with the EPMA at ASU, the Washington State Geoanalytical Lab for geochemical analysis, Spectrum Petrographic for thin section preparation. Samples were collected from the Shasta-Trinity and Modoc National Forests, with acknowledgment of those lands as ancestral tribal lands of the Shasta and Modoc peoples.

TABLE OF CONTENTS

Page

LIST OF TABLES

LIST OF FIGURES

CHAPTER 1

INTRODUCTION

Diffusion chronometry has become a premier tool for investigating timescales associated with magmatic processes. In concert with other petrological and geochemical tools that can constrain magmatic processes and pressure-temperature-composition (P-T-X) conditions in magma storage regions, elemental or isotopic diffusion in minerals and/or melts has become popular within the last five to ten years to assess the timescales of a variety of magmatic processes, including magma mixing to eruption, differentiation and cooling, and more recently, magma ascent rates. Studies using olivine-hosted melt embayments (Lloyd et al. 2014) and melt inclusions (Ruscitto et al. 2010) have determined rapid, syn-eruptive ascent rates (10's of m/s) associated with magma motion in the eruptive column. However, melt embayments and inclusions are subject to post-entrapment modification and therefore, only provide minimum estimates for vapor trapping pressure (Bucholz et al. 2013). Additionally, syn-eruptive rates only reflect magma movement rates during the very last stage of ascent. Shifting focus to trans-crustal ascent rates can better inform ascent rates magmas actually move in the crust. U-series isotopic ratios have the potential to assess crustal magma ascent rates as they reflect the residence time of magma in the crust (Hawkesworth et al. 2004); however, they have limited application to rocks erupted more than a few hundred thousand years ago and it is often difficult to evaluate the depths associated with crustal storage history. So far, only two studies have assessed fully, trans-crustal magma ascent rates. Measurements of Ni diffusion in olivine has been used to assess mantle melting-to-eruption timescales for primitive magmas feeding Irazu volcano, a large stratocone in the

Central American arc (Ruprecht & Plank 2013), which suggest a trans-crustal magma ascent rate (10's of m/day). Similarly, recent diffusion chronometry on olivine constrain transit times of ~10 days from near-Moho conditions to eruption for primitive magmas erupted in northern Iceland, suggesting ascent rates of 100's of m/day (Mutch et al. 2019). Though these studies conclude various trans-crustal magma ascent rates, these rates are integrated histories from the mantle source to the surface. Therefore, these rates are less likely to reflect a specific rate that magma actually traveled. The relative paucity of such estimates leaves many questions as to how characteristic these rates are, as well the relative importance of the primary magma compositions, volatile content, and tectonic setting in dictating these rates. This study utilizes the unique behavior of cinder cone eruptions to more effectively probe the ascent and storage history recorded in primitive arc magmas.

Mafic eruption products from satellite cinder cones in arc volcanic systems have informed our understanding of mantle melting in subduction zones, showing that fractional crystallization of H_2O-rich melts and mantle wedge composition are responsible for andesitic to dacitic compositions in stratovolcanoes (Grove et al. 2005). In this study, we investigate the high-Mg, multiple pyroxene bearing primitive magnesian andesite (PMA) from Mt. Shasta. Though multiple pyroxene andesites and dacites are the volumetrically most dominant product erupted at Mt. Shasta (Grove et al. 2002, 2003, 2005), the PMA has been identified as the primary primitive precursor to these more evolved dacites and andesites in the Mt. Shasta magmatic system (Grove et al. 2005). The PMA erupted with minimal fractionation in a satellite vent ~19km north of the Mt. Shasta summit, effectively skipping the complex plumbing system and multiple

crystallization depths of andesites and dacites erupted in the main edifice. Experiments on the PMA (Grove et al. 2003; Krawczynski et al. 2012) have determined P-T conditions of clinopyroxene and orthopyroxene crystallization, thereby constraining the compositional evolution of the mafic phases and better calibrating the crustal storage conditions experienced by the PMA.

This study utilizes *in situ* mineral geochemistry, whole rock major and minor element geochemistry, thermobarometric calculations, petrographic investigations, and Fe-Mg exchange diffusion chronometry, along with the pre-previously published experimental phase relations, to investigate pre-eruptive storage and crustal ascent rates of the PMA magma. Unlike previous studies assessment of magma ascent rates from an ambiguous mantle source to the surface, this study identifies a magmatic process associated with a specific location in the crust and assesses magma ascent rates during a concise period during the ascent of the PMA prior to cinder cone formation. Results of this study will inform our knowledge the petrogenesis and ascent timescales of both the PMA and more evolved Mt. Shasta andesites and dacites derived from it. In addition, encapsulating ascent timescales better advises volcanic hazard models for Mt. Shasta and provides the grounds for further studies to investigate other arc volcanic systems.

CHAPTER 2

GEOLOGIC SETTING AND PRIOR WORK

2.1 Setting

Mt. Shasta is an andesitic stratocone volcano, located in the southern reach of the Cascades volcanic chain, roughly 130 km northwest of the Lassen Volcanic field, and 60 km west of the Medicine Lake basaltic shield volcano (Fig 1). Tectonic and volcanic activity in the Mt. Shasta region is the product of NW subduction of the Gorda Plate beneath the North American plate at roughly 4 cm/year (Demets et al. 2010). The age of the underlying plate is thought to be relatively young at between 12 and 14 million years old (Green & Harry 1999). The young age of the underlying plate results in the Cascades being one of, if not the, warmest subduction zone on Earth today (Syracuse et al. 2010). These relatively warm thermal parameters and the resulting depths of subducting lithosphere dehydration (e.g, Syracuse et al. 2010; Grove et al. 2002), the location near the southern edge of the Cascades subduction zone (e.g., Till et al. 2013), and potentially the location of the subducting Blanco fracture zone (Emblay & Wilson 1992) all may influence why Mt. Shasta is one of the most productive and hazardous volcanoes in the Cascades today (e.g., Ewart et al. 2018; Till et al. 2019; Managan et al. 2019). Tertiary sandstones, shales, and andesitic volcanics, Mesozoic granites, ultramafics of the Trinity ophiolite, and Paleozoic metasedimentary rocks all uncomformably underlie the Mt. Shasta edifice (Griscom 1980; Blakely et al. 1985; Fuis et al. 1987). Mt. Shasta is thought to have had four major eruptive episodes over the last ~250,000 years (Christiansen et al. 1977), capped by the Hotlum cone that forms the modern summit (14,162’). The Mt. Shasta stratocone is primarily composed of multi-pyroxene andesite

and dacite flows, dacite domes, and pyroclastic flow deposits fed by an H_2O-rich parental magma, the primitive magnesian andesite (PMA) (Grove et al. 2003).

The PMA of Mt. Shasta is exposed at a cinder cone ~19 km north-northeast of the Mt. Shasta summit, in the saddle between Deer mountain and The Whaleback (Fig 2). The cinder cone edifice is densely vegetated and quarried, providing a cross section view of the interior structure and access to the earliest erupted materials. Strong stratifications of red to gray cinders and bombs indicate short lived, oscillatory eruptions, which are common at cinder cones (Pioli et al. 2009). Indurated blocks and bombs consist of porphyritic olivine-augite lava with a dark gray, aphanitic groundmass.

2.2 Cinder Cone Advantage

The pulsatory nature of short lived, small volume eruptions at cinder cones provides a concise window into the mixing history and generation of primitive magmas at mafic arc volcanoes. Their relatively un-evolved eruptive products maintain geochemical signatures imprinted on the magma during its rapid ascent. Prior work has studied the timescales associated with rapid ascent and emplacement of deeply extracted magma at larger, more evolved composite stratocones (Ruprecht & Plank 2013), but little work has been done on primitive arc magmas erupted at cinder cones despite their primitive compositions suggesting a straightforward crustal ascent. While the PMA is the most primitive hydrous magma thought to have erupted in the modern-day Mt. Shasta region (MgO >8.5 wt%; H2O >4.5 wt%), petrography and geochemistry of the crystal cargo do not suggest that it ascended directly from near-Moho depths to erupt, but rather that it experienced a multi-stage history of magma mixing and minimal fractionation.

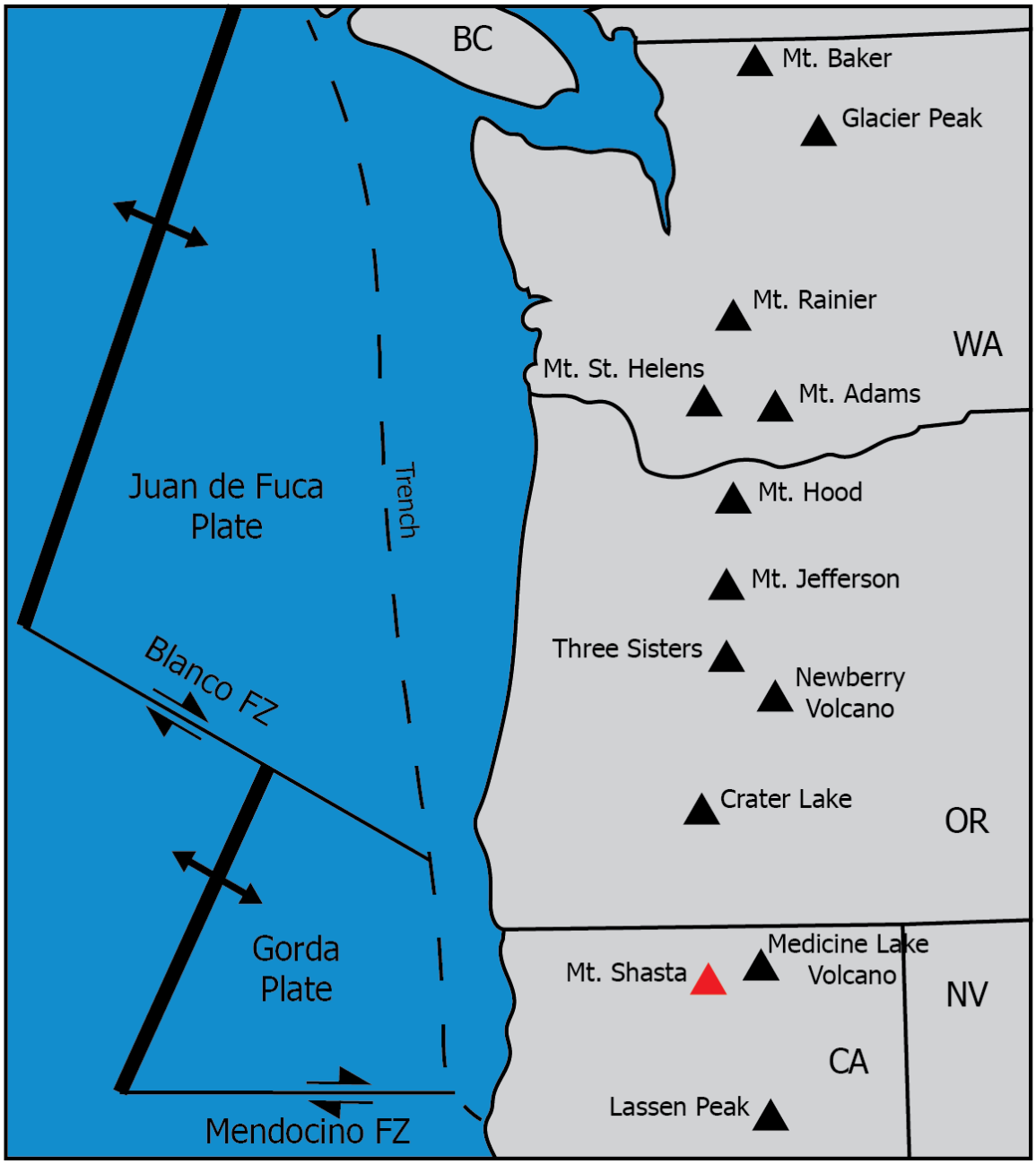

Fig. 1: Map to provide regional context for Mt. Shasta in the greater Cascades range. Each Cascades volcano is signified by a black triangle, with Mt. Shasta in red. Due to the proximity of the Gorda spreading center to the subduction trench, the subducting slab under Mt. Shasta is thought to be one of the warmest on Earth (Syracuse et al. 2010).

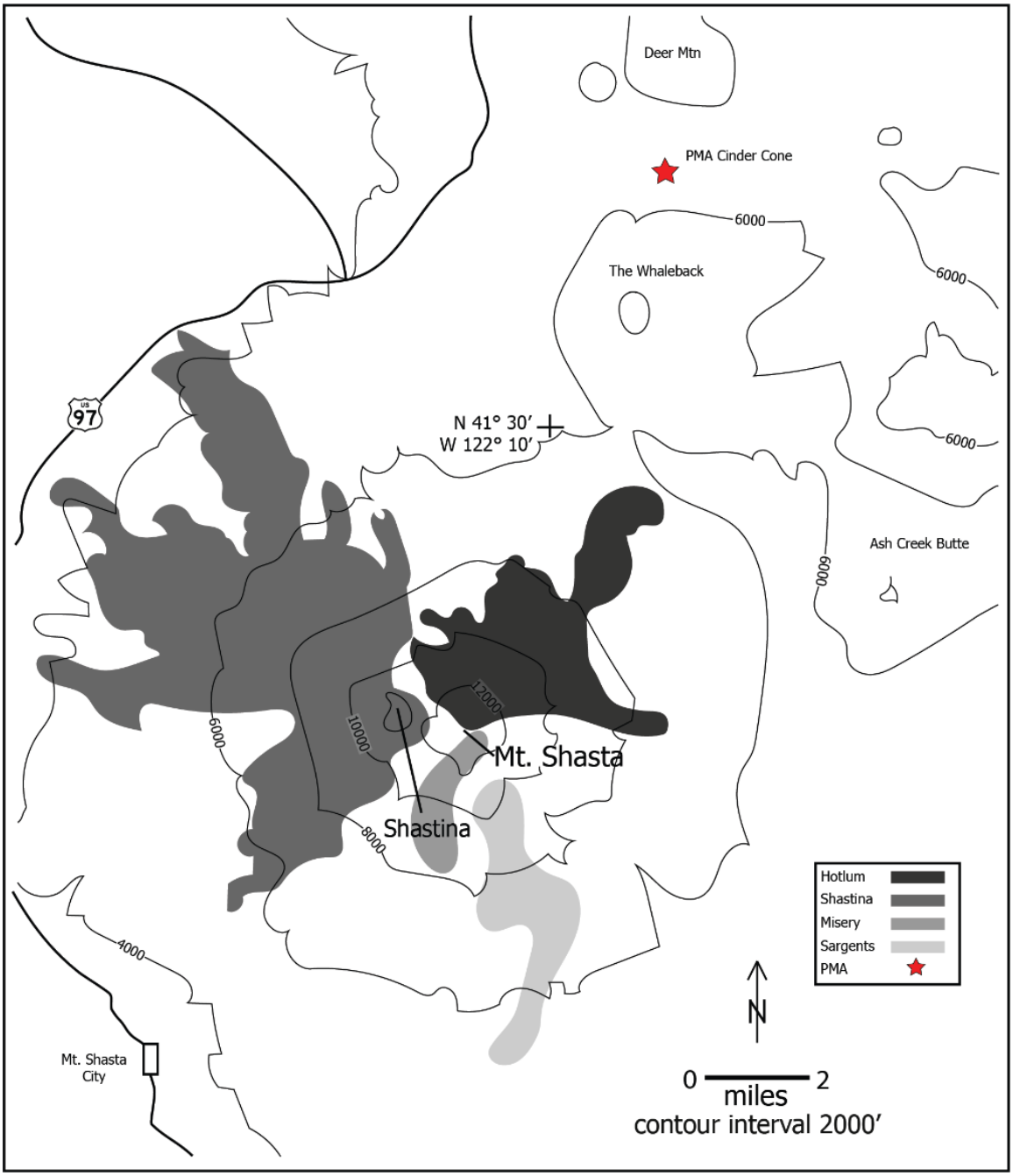

Fig. 2: Map of the Mt. Shasta area showing approximate locations of Quaternary cone building eruptive periods (Baker et al. 1994; Grove et al. 2002). The primitive magnesian andesite (PMA) is highlighted as a red star.

CHAPTER 3

METHODS AND SAMPLES

3.1 Samples

Eight lava samples were collected from the PMA cinder cone. Three minimally vesiculated samples were broken down into 27, 1.2”x 1.2” blanks for thin section processing by Spectrum Petrographics. Petrographic investigations established phenocryst and groundmass assemblages, grain size and abundance, and textural relationships. Fresh cut-offs from thin section preparation were sent for major and trace element geochemistry via X-ray Fluorescence (XRF) and Inductively Coupled Plasma Mass Spectrometry ICP-MS at the Washington State University geoanalytical lab.

3.2 EPMA

Eight polished sections with high pyroxene grain abundance were carbon coated and analyzed for compositional transects of major elements across the outer zone boundary via wave-dispersive spectroscopy using the JXA-8530F Electron Probe Micro-analyzer in the Eyring Materials Center at Arizona State University. EPMA compositional transects were collected at 20 kV and 20 nA using a 1μm beam diameter and 5μm step size to mitigate convolution. Diffusion anisotropy and c-axis growth effects were mitigated by measuring transects orthogonally to the (100) crystallographic plane and parallel to the (010) crystallographic plane. Crystallographic orientations were determined by crystal shape, cleavage, and interference colors. One transect of major element compositions from Mg-rich rims to Fe-rich cores was measured on each of the 21 representative clinopyroxene and 13 representative orthopyroxene phenocrysts. Samples were measured using TAP, TAPH, LIF, LIFH, and PETJ detectors to determine

concentrations of major silicate elements (SiO_2, TiO_2, Al_2O_3, Cr_2O_3, FeO, MnO, MgO, CaO, Na_2O, K_2O). Hornblende, hypersthene, and augite standards were analyzed at the beginning and end of each analytical session to ensure accurately reproduced compositions from the detectors. High-resolution BSE images were taken during analytical sessions for grayscale profile measurements.

3.3 BSE Image grayscale profiles

Gray values of BSE images are a good proxy of Mg# (Mg/(Mg+Fe)) in mafic phenocrysts, such as pyroxenes, with negligible Ca variation (Morgan et al. 2006), justifying the usage of diffusion coefficients for Fe-Mg interdiffusion for clinopyroxene and orthopyroxene. Ca diffusion is slower than Fe-Mg interdiffusion (Cherniak & Dimanov 2010) in pyroxene, and minimal compositional variation in Ca suggests it does not affect the brightness of the BSE image. The equivalency of the BSE contrast and Mg# is corroborated by the Mg# profiles measured in the PMA pyroxene via EPMA to the relative grayscale values extracted for the same transect from BSE images (Fig 3) and has been show in other studies like Petrone et al. 2016. Besides the association of Mg# with gray value in mafic phenocrysts, analytical parameters can also affect the brightness of the resulting BSE image. Though accelerating voltage affects the relative contrast in gray values, the relative difference in gray value between darker, Mg-rich areas and lighter, Fe-rich areas doesn't appear to change. Grayscale value profiles were captured from BSE images with ImageJ® software, orthogonally to the c-axis, in an observational area across the zone boundary, improving statistical accuracy compared to the linear measurement style of EPMA compositional transects. Gray value profiles provide higher

spatial resolution than EPMA compositional transects (~0.5µm pixel resolution of BSE image vs ~5µm EPMA activation volume).

3.4 P-T Constraints

Diffusion is heavily temperature dependent; therefore, temperature was determined via two pyroxene thermobarometry (Putirka 2008). Two-pyroxene thermometry relies on cpx-opx equilibrium pairs. Corresponding cpx-opx pairs were determined by using a $K_D(Fe-Mg)^{cpx-opx} = 1.09 \pm 0.14$ from Putirka 2008. Thermometric calculations were determined within ±60 °C using equation 37 of Putirka 2008, and the barometric calculations were determined within ±3.7 kbar using equation 38 of the same paper. Equilibrium pairs were determined exclusively with pyroxene rim compositions to focus on the conditions of Mg-rich rim growth.

Prior studies have conducted phase equilibrium experiments on the PMA over conditions of 0.1-800 MPa and 940-1250°C (Grove et al. 2003; Krawczynski et al. 2012). Experimental results of Grove et al. 2003 confirmed the PMA's role as the primary primitive precursor of Mt. Shasta lavas, characterizing it as an analogous wet (>4.5 wt% H_2O), primitive arc magma. Experiments from Krawczynski et al. 2012 characterized P-T stability ranges of pyroxene, olivine, plagioclase, and amphibole crystallization. Experimental conditions that produced pyroxene compositions with the lowest standard deviation when compared to average rim compositions of natural pyroxenes were deemed the most likely approximation of P-T conditions during Mg-rich rim growth. Compositional comparison of experimental (Grove et al. 2003; Krawczynski et al. 2012) and our thermobarometric calculations using the natural pyroxene rim compositions were

used to further constrain P-T conditions used for the diffusion modeling described in the next section.

3.5 Diffusion Modeling

Only measured profiles with at least four data points within the concentration/grayscale gradient were used for modeling in order to avoid convolution (Costa & Morgan 2011). To determine the diffusion coefficient, the activation energy and pre-exponential diffusion factors of Fe-Mg interdiffusion in cpx and opx from Müller et al. (2013) and Dohmen et al. (2016) were used, respectively. The appropriate diffusion coefficient was determined over the temperature range with the following Arrhenius-type equation:

$$D = D_0 * \exp\left(\frac{-Q - \Delta V(P - 10^5)}{R * T}\right)$$

Where D is the diffusion coefficient, D_0 is the pre-exponential diffusion factor, Q is the activation energy at 105 Pa, ΔV is the activation volume, P is the pressure in Pa, and R is the gas constant.

The BSE grayscale value profiles were used as a proxy for the Fe-Mg concentration profiles for diffusion chronometry as discussed above. We are only interested in the thermal history recorded in the primary diffusion profile. Consequentially, concentration plateaus either side of the diffusion profile were not included in diffusion modeling, thereby eliminating their impact on the root mean squared misfit of the modeled profile (Fig. 4). For each profile, a planar source with infinite initial concentrations was assumed. The analytical solution to the diffusion equation was used to assess timescales:

$$C_{(t,x)} = C_0 + \left(\frac{C_1 - C_0}{2}\right) * Erfc\left(\frac{x}{2\sqrt{Dt}}\right)$$

where $C_{(t,x)}$ is the composition at point x at time t, C_1 and C_0 are the initial concentrations on each side of the zone boundary, x is the distance from the beginning of the measured profile, D is the diffusivity, and t is the time (Costa and Morgan 2011). The initial concentrations were determined visually and a range of times to model from 1-5 years was input. Using a monte-carlo approach to solve the analytical solution to the diffusion equation, each model was run ten times, with 20000 variable values tested each run. The resulting modeled profile with the smallest misfit from the ten runs was reported as the best fit time and temperature.

3.6 Error Reporting

Typically, diffusion timescale results are reported with symmetrical error values. Though probability distribution functions are often used to determine error, the interpretation of their results do not account for the placement of the best fit time amongst the range of times modeled. A best fit time is found via a monte-carlo approach, where misfit between modeled and measured profiles is minimized over multiple trials. Though this results in a single best fit time and temperature, a range of T-t combinations can solve the analytical solution to the diffusion equation with relatively low misfit (Fig. 5, 6). The low misfit time range results in asymmetric timescale error values because the range of times with low misfit is bounded by zero, resulting in the best fit time not being the median value of the low misfit timescale range (Fig. 6).

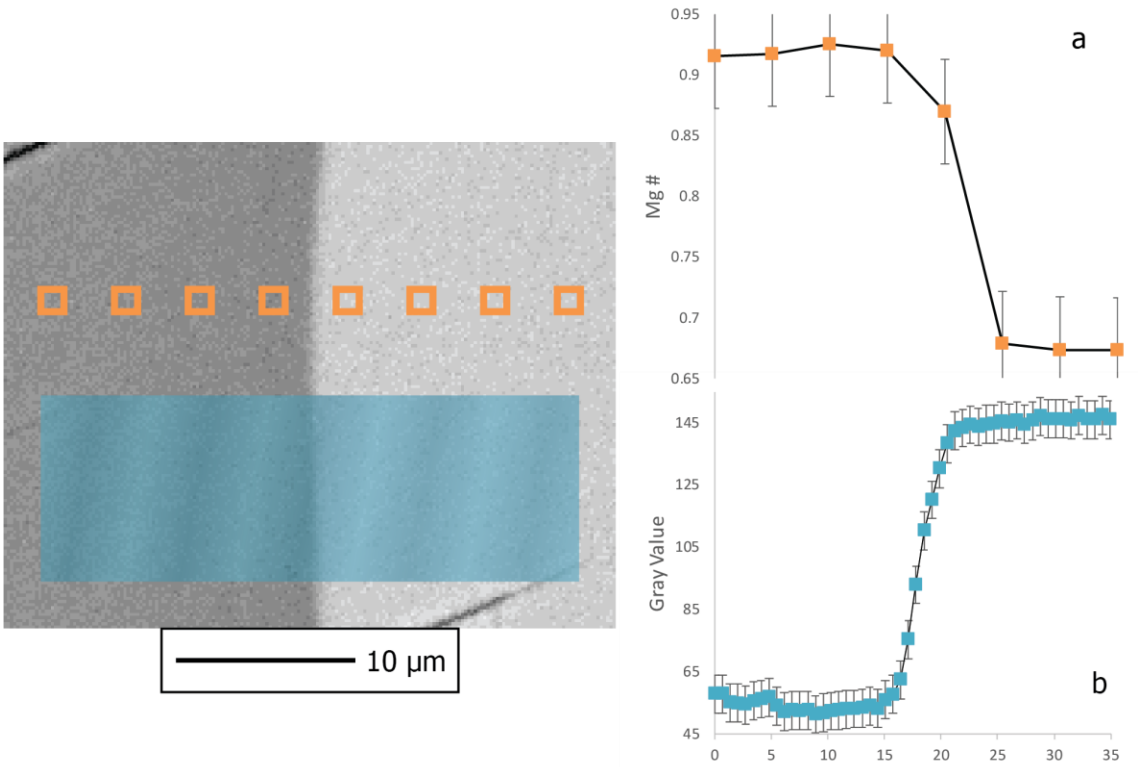

Fig. 3: (a) EPMA compositional profile of Mg# with 5µm spacing used to justify the grayscale profile **(b)** along the orthopyroxene zone boundary. Error bars were calculated with standard error of the mean. BSE grayscale values are used as a proxy for Mg# in clinopyroxene and orthopyroxene with negligible Ca and Al variation across the compositional boundary. Grayscale profiles were used for diffusion modeling as the better spatial resolution produces model profiles with minimal root mean squared misfit.

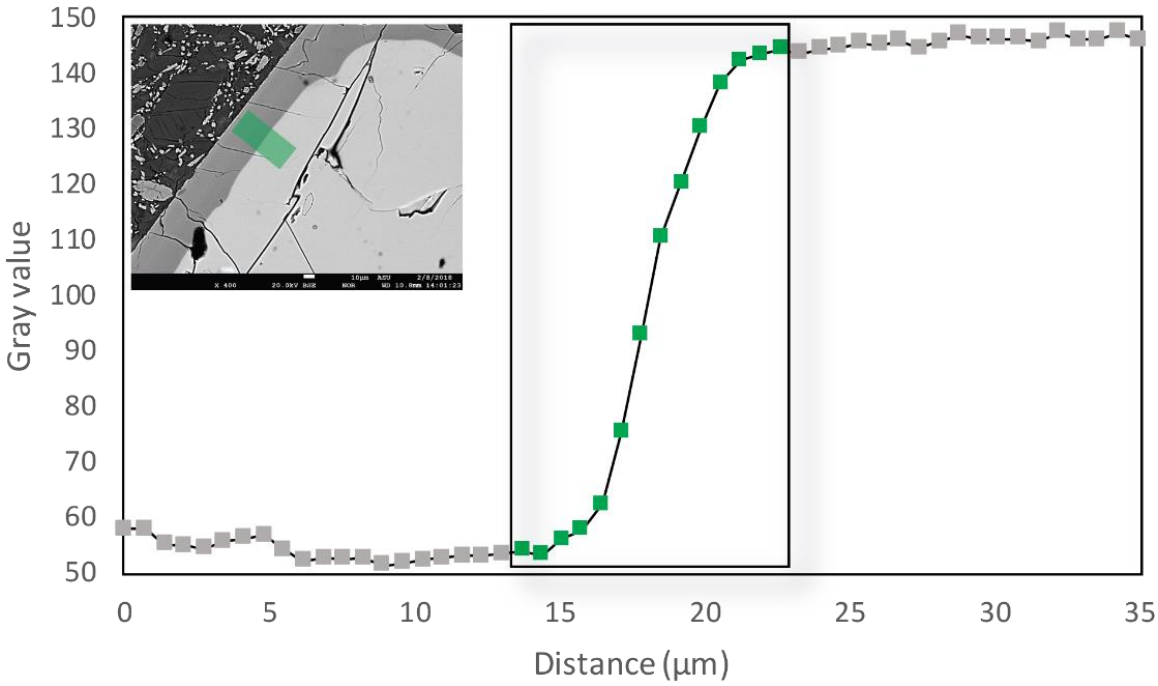

Fig. 4: Example grayscale value profile (dimensionless) vs distance (µm) used for diffusion modeling. Only the rectangular area with highlighted green squares was used for modeling, greyed out squares are concentration plateaus excluded from modeling to produce minimal root mean square misfit. The inset BSE image shows the area of grayscale values captured for this profile.

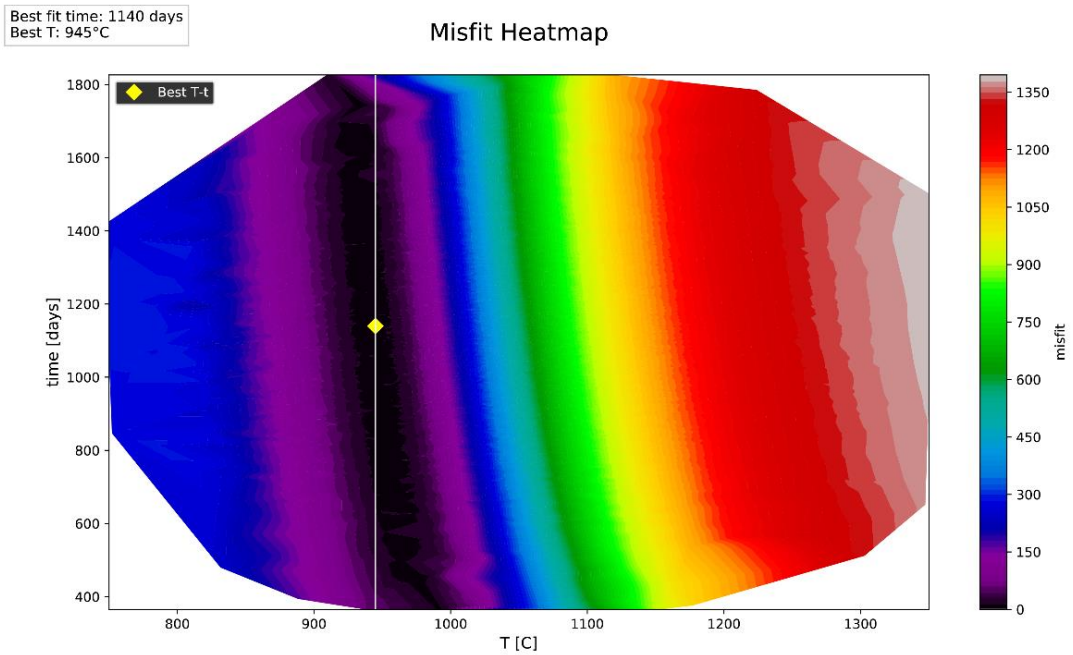

Fig. 5: Misfit heatmap showing the ranges of times and temperatures with associated misfit produced during diffusion modeling with the grayscale value profile of one orthopyroxene phenocryst. Warmer colors are T-t values with higher misfit while cooler colors are T-t values with lower misfit. The yellow diamond represents the best fit time and temperature for this sample while the white line represents where the probability distribution function would plot if viewed from above.

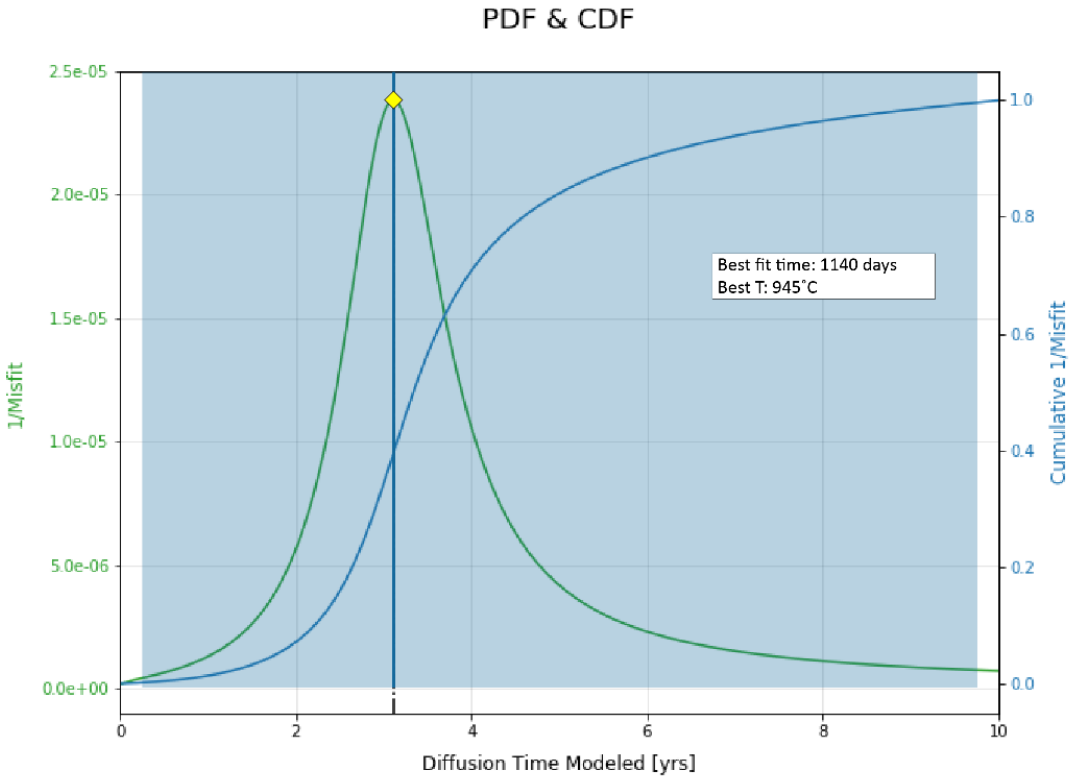

Fig. 6: Plot showing the inverse of the misfit of a diffusion modeling trial. The green line represents the probability distribution function, where the peak represents the best fit time of the model (yellow diamond). The blue plotted line is the cumulative distribution function, where misfit is summed and normalized to 1 to represent the low misfit range of times produced by the model. The transparent blue area represents the 2σ confidence intervals from the best fit time (vertical blue line).

CHAPTER 4

RESULTS

4.1 PMA Lava geochemistry and petrography

The PMA is a calc-alkaline andesite with higher Mg# than any other Mt. Shasta area lavas (Grove et al. 2005)(Fig. 7, Table 1). Polished sections from 3 samples display similar abundances of large (~5-10mm), unzoned olivine phenocrysts and smaller (~2mm) reversely zoned clinopyroxene and orthopyroxene phenocrysts. Normally zoned, submillimeter skeletal olivine and unzoned clinopyroxene and glomerocrysts of intergrown clinopyroxene and orthopyroxene are present in lesser abundances. The groundmass is glassy with plagioclase microlites, pyroxenes, and olivine and does not indicate any flow-alignment. Phenocrysts are mostly euhedral and make up ~15% of the total volume, with glomerocrysts making up <5%.

4.2 Mineral phase major element geochemistry

21 clinopyroxene and 13 orthopyroxene reversely zoned phenocrysts were analyzed for major element profiles. Though core compositions varied between crystal populations, rim compositions were consistent across all clinopyroxene and orthopyroxene examined, with MgO and SiO_2 concentrations of 18-19 wt% and 52-53 wt% and 33-34 wt% and 56-57 wt% respectively (Fig. 8). Olivine phenocrysts are Fo_{90} and do no record the same zoning texture of pyroxene phenocrysts. Groundmass plagioclase is An_{70}.

4.3 Crystal populations

Clinopyroxene, orthopyroxene, and olivine phenocrysts are separated into 3 distinct populations based on major element compositions and textural relationships (Fig.

9). Crystal populations were used to create a conceptual model of the PMA mixing history and the growth of a ubiquitous Mg-rich outer zone on all zoned pyroxene phenocrysts marked the beginning of modeled timescales and ascent rates. Large unzoned olivine, unzoned clinopyroxene, and skeletal olivine are also present, having entered the magma phase assemblage at various points of ascent, as described in section 5.1.

4.4 Thermobarometry & Phase Equilibrium

Temperature and pressure values are inherently coupled with determining timescales and ascent rates of the PMA. Without a reliable temperature range, diffusion modeling would not produce meaningful timescales, rendering the results of this study invalid. Similarly, pressure is used to identify the crystallization depth of the mineral phases in question and allows for a conceptual model of the volcanic plumbing system to be constructed. Therefore, it is of importance to select thermobarometric calculations most likely to produce useful results in preparation for diffusion modeling. Despite the presence of melt inclusions in some zoned pyroxene phenocryst cores, which have applications outside the scope of this study, no glassy groundmass melt inclusions were found. This precludes the use of mineral-liquid thermobarometry, thus the two pyroxene thermobarometer of Putirka (2008) was used to determine a range of P-T conditions for diffusion modeling. This thermobarometer assumes chemical equilibrium between cpx/opx pairs, where the Fe-Mg cpx-opx exchange coefficient is 1.09±0.14. Calculations specifically designed for pyroxenes with Mg# >0.75 returned a pressure-temperature range of 2.6-6.7kbar and 925-1100°C, suggesting mid-crustal crystallization at depths of ~7-20km.

Mid-crustal crystallization is consistent with phase assemblages and compositions from PMA phase equilibrium experiments (Grove et al. 2003; Krawczynski et al. 2012). The compositional alignment between experimental pyroxenes and natural ones suggests P-T conditions of Mg-rich rim growth at 5kbar and 975°C, well within the range determined by two pyroxene thermobarometry from Putirka (2008). Given a temperature range to model from 750-1350°C, average best fit temperatures returned from diffusion modeling are 923°C and 940°C for clinopyroxene and orthopyroxene respectively. In combining these results, we have determined robust pressure and temperature ranges for use in diffusion modeling and conceptualization.

4.5 Diffusion Chronometry Timescales

An important consideration when utilizing diffusion chronometry is determining the magmatic process responsible for producing the concentration profile observed in zoned minerals. The concentration profile can be a result of either slower, fractional growth from slowly mixing magmas or from post-mixing elemental diffusion from rapidly mixing magmas. The distinction is difficult to discern from BSE images alone. Instead, utilizing the concentration profiles of slower diffusing elements like Ca and Cr can distinguish the responsible mechanism. If the profiles of these elements display systematic relaxation across zone boundaries, fractional growth is likely responsible as the Fe-Mg diffusion profiles would be much more relaxed and resulting timescales would be a significant overestimation. In the pyroxenes of from the PMA, the concentration profile of Ca remains relatively flat while the sharp decrease in Cr from rim to core suggests the Mg-rich recharge magma was enriched in Cr, indicative of a primitive source (Fig 11). The behavior of the remaining major elements can be attributed to minor

amounts of Mn substituting for Mg in the Fe-Mg exchange reaction and atomic mass effects. Therefore, we conclude that diffusion following growth of the crystal rim is the primary process responsible for the observed concentration gradients.

Using a Monte Carlo statistical approach to apply the analytical solution to the diffusion equation, we can assess best fit temperatures and times associated with Mg-rich rim growth and pre-eruptive ascent. Plotting the results on probability and cumulative probability functions allows better determination of error associated with timescales derived from this method (Table 2, Fig 6). Minimal standard deviations in thermal and temporal modeling results from Fe-Mg interdiffusion in both clinopyroxene (27°C; 0.59 years) and orthopyroxene suggest (29°C; 0.38 years) experienced similar thermal histories, adding to their credibility. In addition, establishing the behavior of slower diffusion elements like Ca, Ni, and Cr (Cherniak & Dimanov 2010) across the zone boundary can help ensure that the concentration change profile described by the gray value profiles represent elemental diffusion and not fractional growth. The concentration profiles of Ca, Ni, and Cr across the zone boundary were found to be flat, supporting the hypothesis that Fe-Mg interdiffusion did occur. If these profiles did display systematic concentration change behavior, we would expect the measured Fe-Mg profiles to be a result of fractional growth, otherwise the profiles would be much more relaxed and timescales much longer.

Timescale results from diffusion modeling are reported as a range times that produce modeled profiles with relatively low root mean squared misfit. Within that range, a best fit time and temperature is reported for each grayscale profile, in this case one per phenocryst (see Fig 6). Diffusion modeling of Fe-Mg interdiffusion in

clinopyroxene and orthopyroxene suggest timescales of $2.9^{+6.6}_{-2.7}$ years and $2.9^{+6.4}_{-2.2}$ years, respectively. See Table 2 for diffusion results.

Table 1: Bulk major element geochemistry of Mt. Shasta primitive magnesian andesite

SiO_2	57.58
TiO_2	0.58
Al_2O_3	14.51
FeO*	5.65
MnO	0.10
MgO	8.55
CaO	8.02
Na_2O	3.00
K_2O	0.75
P_2O_5	0.12
LOI %	0.35
Sum	98.86

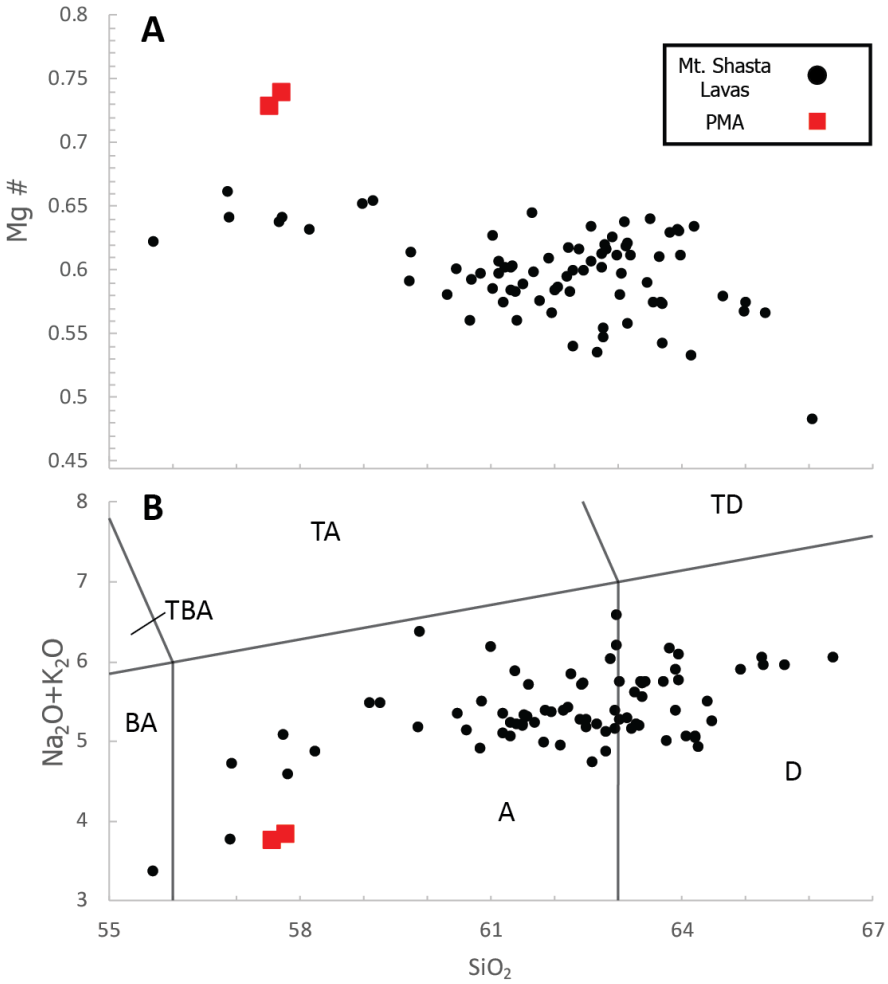

Fig. 7: Bulk geochemistry plots of PMA (red squares) compared to other Mt. Shasta lavas (black circles) (Grove et al. 2005). (A) Mg# vs SiO_2 (B) Total alkalis vs SiO_2; BA *basaltic andesite*, A *andesite*, D *dacite*, TD *trachy-dacite*, TA *trachy-andesite*, TBA *trachy-basaltic andesite*

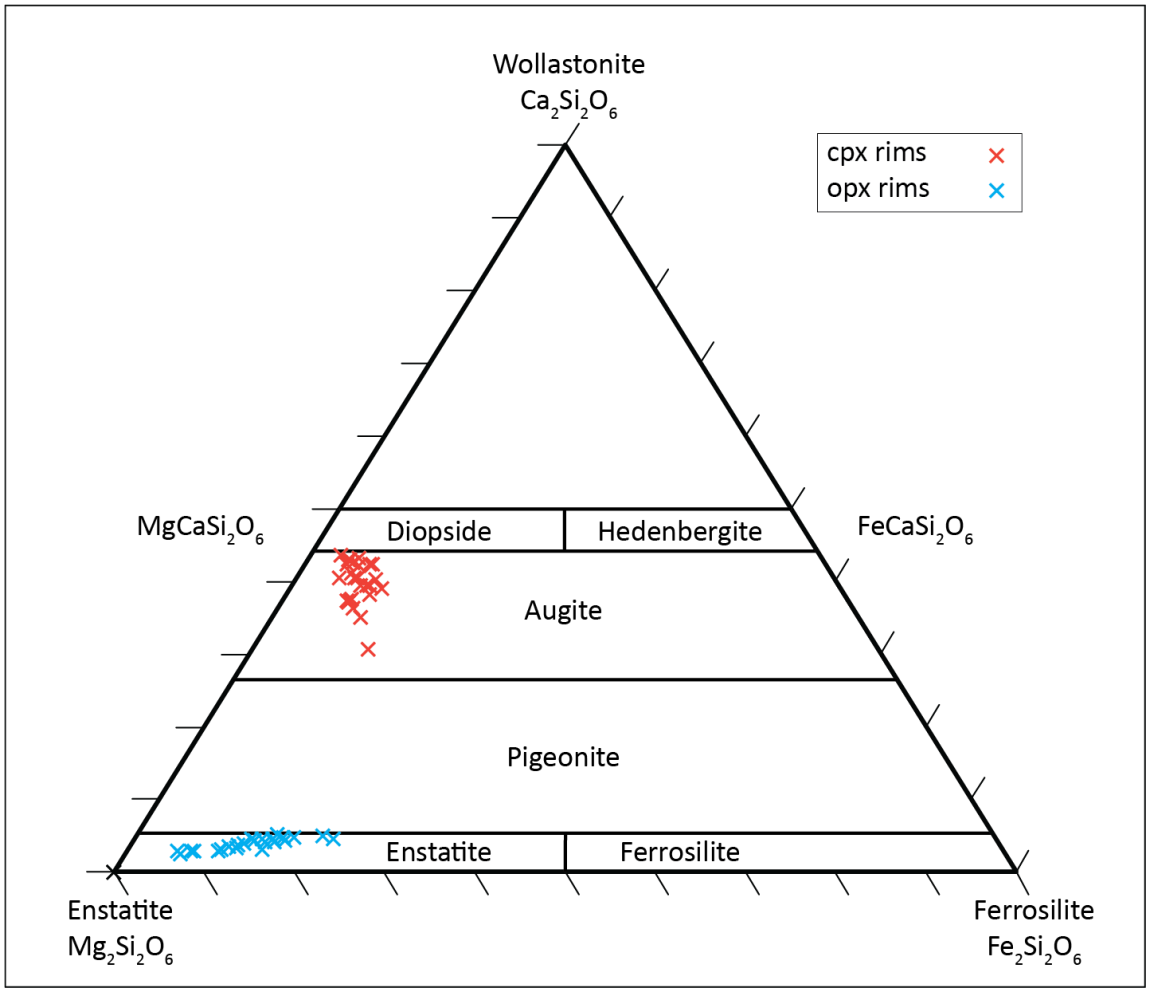

Fig. 8: Pyroxene ternary diagram showing clinopyroxene (red) and orthopyroxene (blue) rim compositions

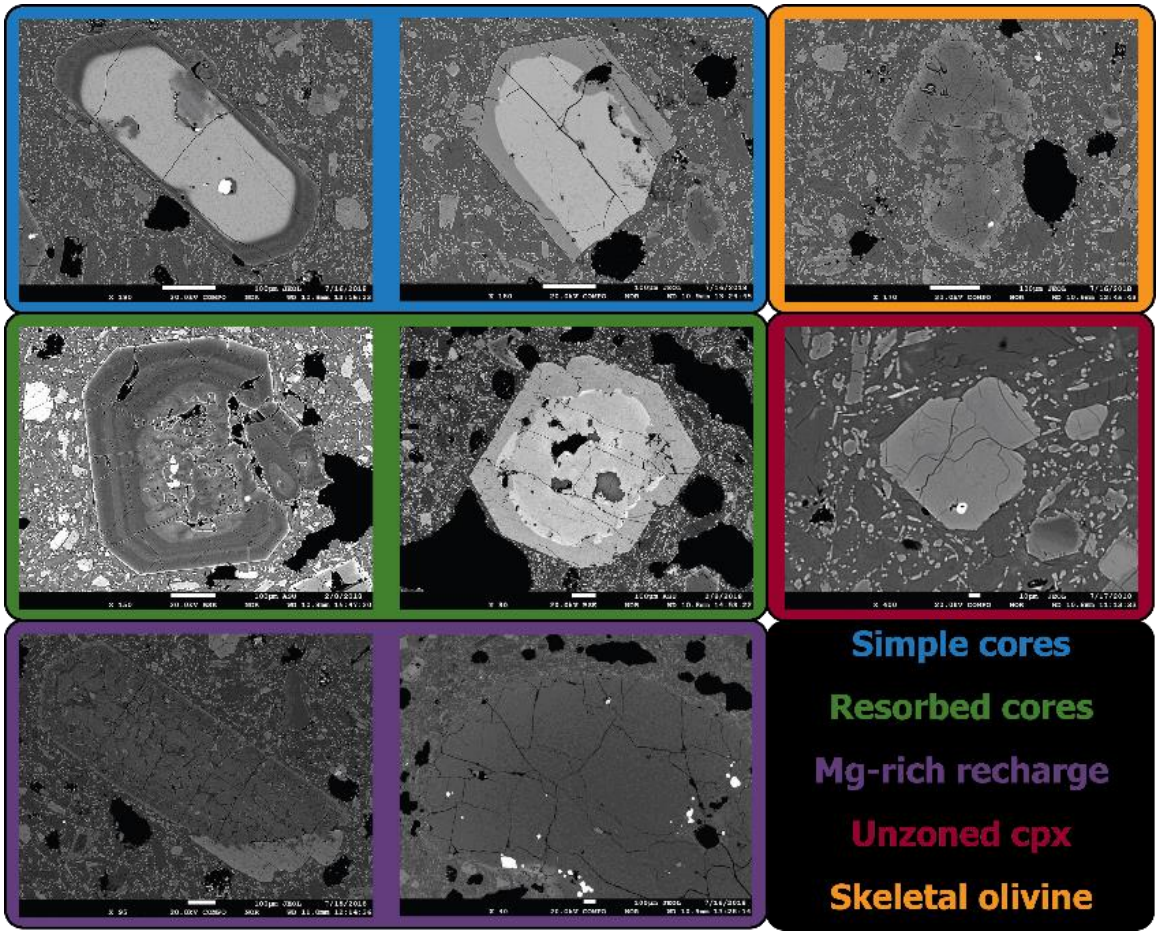

Fig. 9: BSE images of phase populations. Highlighted in blue are pop. 1 pyroxenes with simple cores (opx left; cpx right). Highlighted in green are pop. 2 pyroxenes with resorbed cores (opx left; cpx right). Highlighted in purple are phases from the Mg-rich recharge (opx left; ol right). Highlighted in red is an unzoned cpx and highlighted in orange is a skeletal olivine.

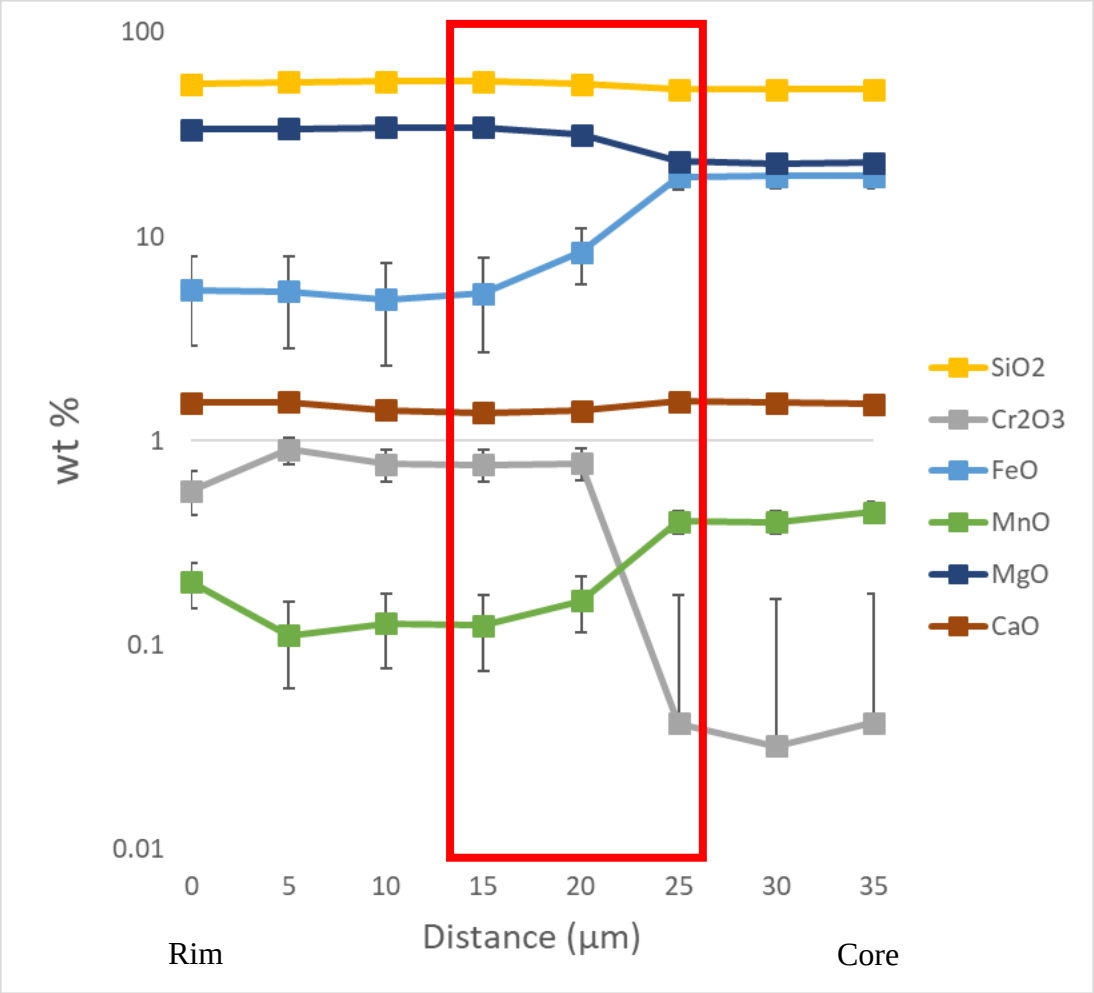

Fig 10: Major element concentration profiles of representative, reversely zone orthopyroxene phenocryst with rim compositions of the left and core on the right. Error bars are standard error of the mean. The primary elemental exchange is between Fe and Mg, though Mn can also be involved in the exchange reaction. Though Cr displays a concentration change, it is not over the full width of the diffusion profile (highlighted in red). Less evolved magmas tend to be enriched in Cr, suggesting the recharge magma was more primitive than the more evolved version it mixed with to form Mg-rich rims on pyroxene phenocrysts.

Table 2: Best fit times and temperatures from diffusion modeling

Sample	Best time (years)	Positive error (years)	Negative error (years)	Best temperature (°C)
Clinopyroxene				
01-cpx1	2.93	5.85	1.91	907
01-cpx2	2.93	4.84	1.35	897
01-cpx3	3.28	4.24	1.71	884
04-cpx1	3.12	4.09	1.46	923
04-cpx4	2.75	5.51	1.34	930
04-cpx5	2.69	5.7	1.41	944
04-cpx6	1.57	6.57	0.81	940
08-cpx1	3.26	5.34	1.86	938
08-cpx2	3.43	4.47	1.57	974
08-cpx3	2.78	4.5	1.17	993
11-cpx1	2.25	5.8	1.09	920
11-cpx2	2.94	5.56	1.59	934
11-cpx3	3.46	5.05	2.36	905
12-cpx2	3.45	5.23	1.95	923
12-cpx4	2.84	4.65	1.39	940
12-cpx7	4.5	4.71	2.74	908
16-cpx1	2.99	5.81	1.88	896
16-cpx2	3.25	4.96	1.66	906
16-cpx3	2.87	5.34	1.7	887
22-cpx1	1.98	4.4	0.87	898
23-cpx1	3.25	5.57	1.97	928
Average	2.98			923
Max positive err	6.57			
Max negative err	2.74			
Orthopyroxene				
01-opx1	2.85	6.44	2.05	937
04-opx1	2.77	5.39	1.43	948
04-opx3	2.59	4.59	1.24	985
04-opx4	3.32	4.56	1.58	911
08-opx2	2.35	5.5	1.38	880
08-opx3	3.1	5.57	1.81	919
11-opx1	3.66	5.54	2.24	921
11-opx2	3.43	5.4	2.08	930
12-opx2	3.05	5.43	1.68	945
16-opx1	2.62	4.96	1.23	967
16-opx2	2.97	4.04	1.24	945
22-opx2	2.55	5.03	1.28	982
22-opx3	2.82	5.66	1.55	948
Average	2.93			940
Max positive err	6.44			
Max negative err	2.24			

Table 3: Pyroxene rim major element geochemistry

Sample	SiO_2	TiO_2	Al_2O_3	Cr_2O_3	FeO	MnO	MgO	CaO	Na_2O	K_2O
Pop. 1 cpx										
04-cpx1	53.2885	0.200417	1.8798	1.01801	4.1059	0.113202	18.4974	20.5306	0.356314	0.009458
04-cpx7	53.4399	0.270674	2.56812	1.12231	4.13391	0.133442	17.7034	21.3351	0.212792	0.012278
04-cpx8	54.195	0.207217	2.03413	1.026	4.03963	0.135928	18.8974	20.5635	0.232452	0.006742
01-cpx3	52.2813	0.205457	1.92414	0.999241	4.01653	0.128151	18.2443	21.0131	0.220625	0.015749
04-cpx6	53.3452	0.210072	2.12891	1.0493	3.77637	0.086709	17.8062	20.9896	0.248873	0.006352
08-cpx3	53.3417	0.222669	2.10281	1.0839	3.89417	0.102736	18.3187	20.8679	0.23644	0.011218
11-cpx1	53.3276	0.220786	1.92628	0.937628	3.9337	0.151975	18.4961	21.1743	0.181202	
11-cpx2	52.9078	0.349091	3.19254	0.5392	4.70581	0.131607	17.941	20.5306	0.365671	0.012303
12-cpx1	54.0922	0.217252	1.36483	0.37457	5.35643	0.172081	19.8341	18.1885	0.137568	0.00992
16-cpx1	52.3643	0.226083	2.16797	1.13777	4.03637	0.106423	18.1221	21.378	0.234292	0.008685
16-cpx2	54.1782	0.216784	1.64912	0.548282	4.55211	0.130017	19.1681	20.3667	0.190394	0.017724
16-cpx3	52.5147	0.316405	2.11032	0.519311	4.79763	0.150861	17.5924	20.7973	0.281634	0.06717
Pop. 2 cpx										
01-cpx1	52.7062	0.266294	2.19334	0.604685	4.88769	0.128994	19.1045	19.6717	0.19443	0.006068
11-cpx3	53.5351	0.211035	1.98071	1.04795	4.10972	0.130279	18.8147	20.4512	0.218984	0.008316
22-cpx1	54.37512	0.214255	2.097948	0.94073	4.23443	0.134002	18.8183	20.10663	0.258172	0.010498
01-cpx2	53.0485	0.249751	2.29044	1.01367	4.14528	0.094966	18.5463	20.6461	0.236195	0.009091
04-cpx4	52.9282	0.2039	1.89005	1.02105	3.75064	0.147047	18.186	21.2372	0.207876	0.006581
04-cpx5	53.0781	0.222997	2.13111	1.19344	3.94368	0.118763	18.1025	20.7197	0.268318	0.018961
08-cpx1	53.8223	0.170066	1.87459	1.01249	3.84645	0.107279	18.7924	20.0126	0.272136	0.019764
08-cpx2	53.2914	0.211091	1.91623	0.976353	4.28659	0.09798	18.8214	19.617	0.233718	0.009057
12-cpx4	53.0569	0.175684	1.69739	0.710715	4.06873	0.122311	18.5621	20.1246	0.217731	0.010904
12-cpx7	53.5667	0.205391	1.97589	0.892326	4.06703	0.123816	18.5048	20.4201	0.219532	0.014354
23-cpx1	53.943	0.232029	2.04099	1.06379	4.229	0.125961	18.8764	20.1387	0.212922	0.015536
Pop. 1 opx										
04-opx1	56.886	0.082075	1.53248	1.02315	5.36049	0.126209	33.9732	1.58223	0.044681	0.009197
04-opx4	57.1026	0.050675	1.51834	0.879493	5.33759	0.123348	33.6122	1.63019	0.069613	0.019317
12-opx2	56.905	0.072952	1.56614	0.902064	5.37359	0.111238	33.6382	1.54375	0.02825	0.012891
16-opx1	57.0927	0.069691	1.46015	0.747691	5.20623	0.13844	34.2946	1.58454	0.033566	0.013571
Pop. 2 opx										
04-opx3	57.4395	0.044968	1.33192	0.849331	4.84886	0.122782	34.5243	1.44812	0.033168	0.00742
11-opx1	56.5976	0.071214	1.60995	0.795731	5.5195	0.116802	33.6466	1.84559	0.04937	0.006328
22-opx3	58.212	0.069794	1.4262	0.929811	5.13793	0.124023	33.9121	1.48096	0.057447	0.008561
Mg-rich recharge opx										
01-opx1	56.7696	0.068148	0.978364	0.583798	5.71048	0.1425	34.052	1.42942	0.024321	0.007449
04-opx5	57.4299	0.088311	1.48775	0.679154	6.7108	0.145353	32.82	1.96634	0.041727	0.017199
08-opx3	56.5271	0.079648	1.42995	0.702276	6.41715	0.164306	33.3659	1.63118	0.025343	0.006167
08-opx4	56.7603	0.090251	1.52859	0.605341	6.77566	0.144968	32.7896	1.6067	0.026419	0.013016
11-opx2	55.9109	0.070038	1.24669	0.794505	4.8033	0.119865	34.3263	1.41836	0.032915	0.017466
12-opx3	56.6292	0.106767	1.48091	0.486297	7.25854	0.127375	32.2866	1.55493	0.028271	0.004681
12-opx4	57.2666	0.108161	1.11491	0.385539	6.73817	0.167717	33.1025	1.77183	0.030446	0.018105
16-opx2	56.4243	0.077065	0.931107	0.401267	6.46368	0.110731	32.6667	2.15092	0.041753	0.010366
22-opx1	57.0262	0.129112	1.99199	0.266738	7.66355	0.168403	31.7014	1.87914	0.041753	

CHAPTER 5

DISCUSSION

5.1 Magma Mixing & Storage History

Combining the petrographic, thermobarometric, and analytical geochemical results provides a framework for constructing a conceptual model of the volcanic plumbing system of the Mt. Shasta primitive magnesian andesite. Our results suggest multiple mixing events occurred involving more and less evolved versions of the primitive PMA magma between 925-1100°C and 2.6-6.7kbar, or ~7-20km. The most robust evidence of mixing is the presence of multiple, major element compositionally and texturally unique pyroxene core populations that all share a compositionally ubiquitous Mg-rich outer zone at 975°C and 5kbar. Combining these pyroxene populations requires multiple mixing and growth events (Fig. 10). (1) Prior to Mg-rich rim growth, simple and resorbed clinopyroxene and orthopyroxene cores are mixed in the mid crust. (2) Following the initial mixing, a primitive, Mg-rich version of the PMA containing pyroxene phenocrysts and large, unzoned olivine phenocrysts mixed with the other two populations. Thermobarometric and experimental constraints on pressure and temperature suggest this occurred at ~15km depth. (3) After mixing, ascent of the now hotter and relatively homogenous magma causes decompression and undercooling, leading to the crystallization of unzoned clinopyroxene phenocrysts. (4) Upon eruption, skeletal olivine crystals are formed, and groundmass pyroxene, olivine, and plagioclase are crystallized.

5.2 Ascent Timescales

Previously, primitive arc magmas were thought to have a rapid and simple ascent from moho depth to surface (Grove et al. 2005). Though previous studies have estimated trans-crustal ascent rates, the results of this study represent some of the earliest estimations of magma ascent from mixing at a specific depth to eruption. These results suggest that a multistage history of magma mixing, storage, and fractionation for the Mt. Shasta PMA. From Mg-rich rim growth to eruption, the PMA went from ~5kbar, or 15km, to eruption in under 10 years, or ~$2.9^{+6.5}_{-2.5}$ years. Comparing the depth and timescale provides an estimate for ascent rate velocities of 2-11km/year. It must be recognized that these ascent rates are minimum values determined solely by the amount of time diffusion occurred in the pyroxene phenocrysts. The PMA could have ascended more rapidly with longer periods of storage at various depths but would have had to move at a minimum constant rate of 2-11km/year to transit that distance. Another issue that must be address is the minor amount of resorption experienced by the subhedral pyroxene cores before after the magmas were mixed, before Mg-rich rim growth began. This has the effect of causing the timescale clock to begin at the moment of Mg-rich rim growth as opposed to Mg-rich, primitive recharge.

Often, assessments of ascent rates focus on syn-eruptive rates captured by melt embayment volatile gradients (Lloyd et al. 2014), and report rates much faster than described by this study. However, compared to other assessments of trans-crustal ascent rates (Table 4), the PMA resides on the fast end of the spectrum for hydrous arc magmas that might otherwise be stored and differentiated to more evolved andesite-dacite in the complex plumbing systems of major stratocone magmas. Though the tectonic setting is

similar, the primitive and consequentially more dense nature of the PMA is likely why the ascent rates are slightly slower than those determined from more silicic, less dense magmas reported in Ruprecht & Plank (2013). As for why the PMA ascent rate is slower than those reported in Iceland by Mutch et al. (2019), the tectonic setting is likely to blame. The alignment of tectonic forces and gradients of pressure throughout the crust differ greatly between the divergent boundary setting of Iceland and convergent setting of Mt. Shasta. Similarly, the complex relationship between plume and mid-ocean ridge mantle melting in Iceland likely has a strong effect on the primary magma composition and tectonic stresses in the area, accelerating decompression rates of magmas in that system.

5.3 Diffusion Modeling & Volcanic Monitoring

The mixing-to-eruption timescales imprinted on zoned minerals can inform not only magma ascent rates but also volcanic hazard mitigation. The magmatic processes responsible for compositional zoning are often recharge events that mix new melt and mineral compositions into magmatic plumbing systems. Long-period seismicity temporally linked to magma recharge events can start eruption timers if paired with ascent timescales from diffusion chronometry (Saunders et al. 2012). With increased seismic resolution at high threat volcanoes, eruption forecasting could be extended from the order of weeks to years depending on the mixing-to-eruption timescales assessed from diffusion chronometry on zoned minerals.

Table 4: Summary of ascent rates from other studies

Method	Ascent rates
Xenolith bearing magmas (Blatter et al. 1998)	26 km/day
Olivine-hosted melt emabayments (Lloyd et al. 2014)	15 m/s
U-series isotopes (Mckenzie 2000)	10 km/year
Ni zonation in olivine (Ruprecht & Plank 2013)	68 m/day
(Mutch at al. 2019)	8 km/day
Fe-Mg interdiffusion in cpx and opx (This study)	2-11 km/year

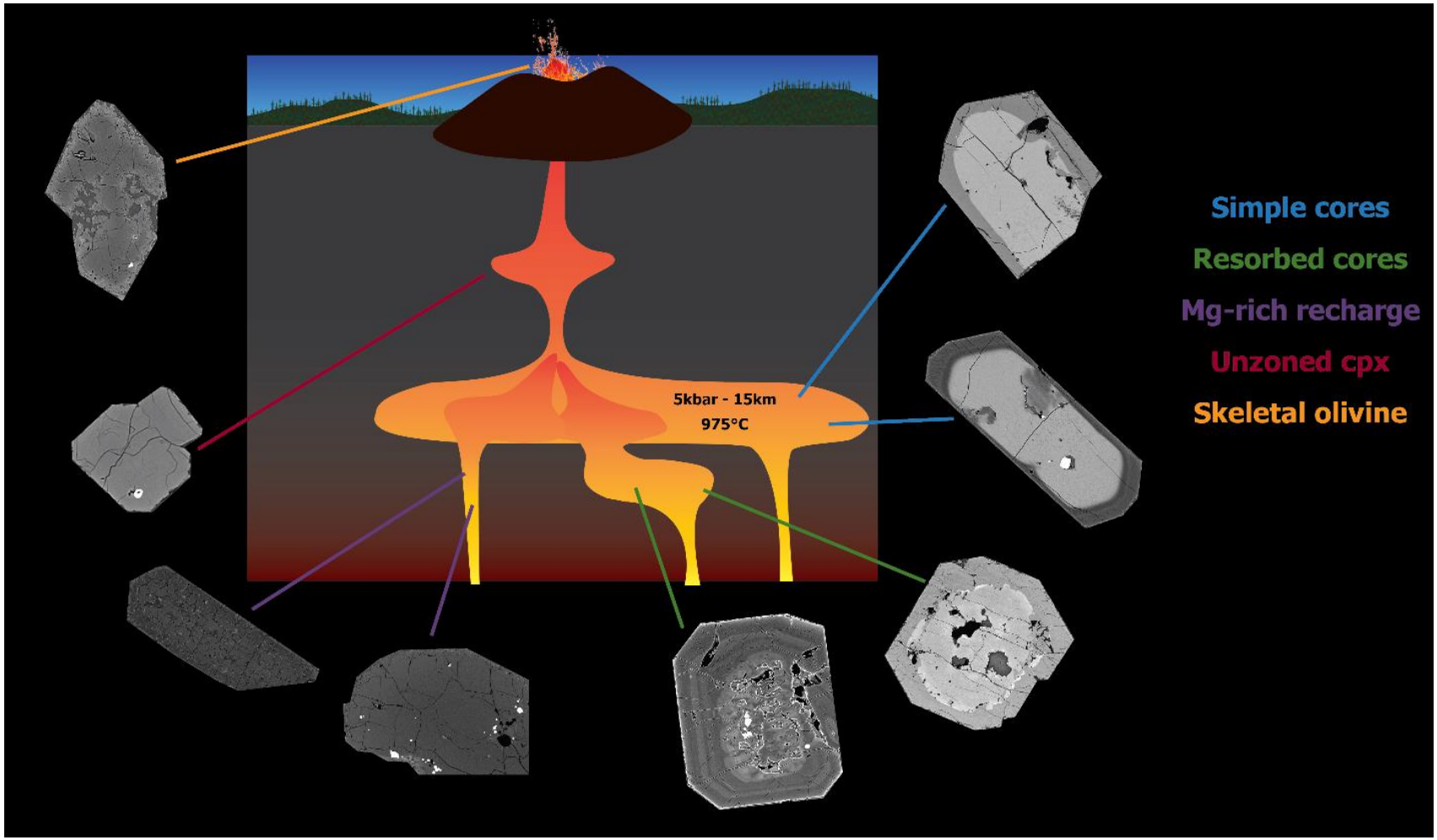

Fig. 11: Schematic figure of proposed mixing history. Lines are color coordinated with the associated crystal population and point to the original crystallization location of that phenocryst population.

CHAPTER 6

CONCLUSIONS

Though originally thought to have erupted as a result of magma sourced from deep in the mantle, ascending through the crust with minimal storage and evolution, the Mt. Shasta primitive magnesian andesite displays evidence of a more complex history. Petrographic and geochemical analyses reveal a phenocryst assemblage with chemical zoning and varying degrees of fractionation. To investigate the pre-eruptive history and ascent timescales of the PMA we utilize in situ mineral geochemistry, whole rock major and minor element geochemistry, thermobarometric calculations, experimental phase relations, petrographic investigations, and Fe-Mg exchange diffusion chronometry. Before determining ascent rates and timescales, a conceptual model of the PMA volcanic plumbing system was created. Using petrography and EPMA major element geochemical analysis, multiple distinct pyroxene and olivine crystal populations were identified via textures and major element geochemistry shared amongst each population. Reverse zonation was identified in four pyroxene populations, where Fe-rich cores of varying composition all grew a compositionally homogenous, Mg-rich rim, suggesting pyroxene cores experienced magma mixing prior to Mg-rich rim growth. Pyroxene populations laid a framework for constructing a conceptual model, while thermobarometric calculations (Putirka 2008) estimated P-T constraints to 2.6-6.7kbar and 925-1100°C and phase equilibrium experiments further constrained P-T conditions to 5kbar and 975°(Grove et al. 2003; Krawczynski et al. 2012). Robust P-T constraints were used in diffusion chronometry, where we determined timescales and rates of magma flux through the PMA volcanic plumbing system. Using the analytical solution to the

diffusion equation (Costa & Morgan 2011), 21 and 13 reversely zoned clinopyroxene and orthopyroxene, respectively, were measured with the EPMA for major element profiles across the zone boundary. With negligible Ca, Ni, and Cr profiles, Fe-Mg interdiffusion was found to be the only elemental system with any meaningful diffusion over short timescales. BSE images of pyroxene phenocrysts were converted into gray value profiles, providing higher spatial resolution than EPMA major element profiles for use in diffusion chronometry. Using both clinopyroxene and orthopyroxene to probe pre-eruptive history and conditions ensures that the distinct phenocryst populations underwent the same thermal and temporal evolution. The results of diffusion modeling lead to these conclusions:

1. Primitive arc magmas, like the PMA, experience pre-eruptive storage less complex than main stratocone lavas but more complex than direct pipelines from the mantle.
2. Transit of the PMA volcanic plumbing system takes **~2.** $\mathbf{9^{+6.5}_{-2.5}}$ **years** years at minimum ascent rates of **2-11 km/year.**

Though other studies have looked at ascent rates of magma, they typically do so focus on syn-eruptive rates rather than magma flux rates through volcanic plumbing systems (Table 3). While those rates are important for the very final moments of a magma's pre-eruptive history, the timescales assessed in this study represent a quantification of the time required for magma to move through a volcanic plumbing system after a magmatic event, in this case Mg-rich recharge and mixing. Overall, the combined results of this study provide new estimates of the pre-eruptive history, rates, and evolution of the Mt. Shasta primitive magnesian andesite, enriching our

understanding primitive arc magma petrogenesis and informing volcanic hazard models for monogenetic, cinder cone eruptions in the Southern Cascades.

REFERENCES

Baker, M. B., Grove, T. L., & Price, R. (1994). Primitive basalts and andesites from the Mt. Shasta region, N. California: products of varying melt fraction and water content. *Contributions to Mineralogy and Petrology*, *118*(2), 111-129.

Blakely, R. J., Jachens, R. C., Simpson, R. W., & Couch, R. W. (1985). Tectonic setting of the southern Cascade Range as interpreted from its magnetic and gravity fields. *Geological Society of America Bulletin*, *96*(1), 43-48.

Blatter, D. L., & Carmichael, I. S. (1998). Hornblende peridotite xenoliths from central Mexico reveal the highly oxidized nature of subarc upper mantle. *Geology*, *26*(11), 1035-1038.

Bucholz, C. E., Gaetani, G. A., Behn, M. D., & Shimizu, N. (2013). Post-entrapment modification of volatiles and oxygen fugacity in olivine-hosted melt inclusions. *Earth and Planetary Science Letters*, *374*, 145-155.

Cherniak, D. J., & Dimanov, A. (2010). Diffusion in pyroxene, mica and amphibole. *Reviews in Mineralogy and Geochemistry*, *72*(1), 641-690.

Christiansen, R. L., Kleinhampl, F. J., Blakely, R. J., Tuchek, E. T., Johnson, F. L., & Conyac, M. D. (1977). *Resource appraisal of the Mt. Shasta wilderness study area, Siskiyou County, California* (No. USGS-OFR-77-250). Geological Survey, Menlo Park, CA (USA).

Costa, F., & Morgan, D. (2011). Time constraints from chemical equilibration in magmatic crystals. *Timescales of magmatic processes: from core to atmosphere. Wiley, Chichester*, 125-159.

DeMets, C., Gordon, R. G., & Argus, D. F. (2010). Geologically current plate motions. *Geophysical Journal International*, *181*(1), 1-80.

Dohmen, R., Ter Heege, J. H., Becker, H. W., & Chakraborty, S. (2016). Fe-Mg interdiffusion in orthopyroxene. *American Mineralogist*, *101*(10), 2210-2221.

Embley, R. W., & Wilson, D. S. (1992). Morphology of the Blanco transform fault zone-NE Pacific: Implications for its tectonic evolution. *Marine geophysical researches*, *14*(1), 25-45.

Ewert, J. W., Diefenbach, A. K., & Ramsey, D. W. (2018). *2018 update to the US Geological Survey national volcanic threat assessment* (No. 2018-5140). US Geological Survey.

Fuis, G. S., Zucca, J. J., Mooney, W. D., & Milkereit, B. (1987). A geologic interpretation of seismic-refraction results in northeastern California. *Geological Society of America Bulletin*, *98*(1), 53-65.

Green, N. L., & Harry, D. L. (1999). On the relationship between subducted slab age and arc basalt petrogenesis, Cascadia subduction system, North America. *Earth and Planetary Science Letters*, *171*(3), 367-381.

Griscom, A. (1980). Cascade Range and Modoc Plateau. *Bull. Calif. Div. Mines Geol*, *205*, 36-38.

Grove, T., Parman, S., Bowring, S., Price, R., & Baker, M. (2002). The role of an H 2 O-rich fluid component in the generation of primitive basaltic andesites and andesites from the Mt. Shasta region, N California. *Contributions to Mineralogy and Petrology*, *142*(4), 375-396.

Grove, T. L., Elkins-Tanton, L. T., Parman, S. W., Chatterjee, N., Müntener, O., & Gaetani, G. A. (2003). Fractional crystallization and mantle-melting controls on calc-alkaline differentiation trends. *Contributions to Mineralogy and Petrology*, *145*(5), 515-533.

Grove, T. L., Baker, M. B., Price, R. C., Parman, S. W., Elkins-Tanton, L. T., Chatterjee, N., & Müntener, O. (2005). Magnesian andesite and dacite lavas from Mt. Shasta, northern California: products of fractional crystallization of H 2 O-rich mantle melts. *Contributions to Mineralogy and Petrology*, *148*(5), 542-565.

Hawkesworth, C., George, R., Turner, S., & Zellmer, G. (2004). Time scales of magmatic processes. *Earth and Planetary Science Letters*, *218*(1-2), 1-16.

Krawczynski, M. J., Grove, T. L., & Behrens, H. (2012). Amphibole stability in primitive arc magmas: effects of temperature, H 2 O content, and oxygen fugacity. *Contributions to Mineralogy and Petrology*, *164*(2), 317-339.

Lloyd, A. S., Ruprecht, P., Hauri, E. H., Rose, W., Gonnermann, H. M., & Plank, T. (2014). NanoSIMS results from olivine-hosted melt embayments: magma ascent rate during explosive basaltic eruptions. *Journal of Volcanology and Geothermal Research*, *283*, 1-18.

McKenzie, D. (2000). Constraints on melt generation and transport from U-series activity ratios. Chemical Geology, 162(2), 81-94.

Mangan, M., Ball, J., Wood, N., Jones, J. L., Peters, J., Abdollahian, N., ... & Pridmore, C. (2019). California's exposure to volcanic hazards (No. 2018-5159). US Geological Survey.

Müller, T., Dohmen, R., Becker, H. W., Ter Heege, J. H., & Chakraborty, S. (2013). Fe–Mg interdiffusion rates in clinopyroxene: experimental data and implications for Fe–Mg exchange geothermometers. *Contributions to Mineralogy and Petrology*, *166*(6), 1563-1576.

Mutch, E. J., Maclennan, J., Shorttle, O., Edmonds, M., & Rudge, J. F. (2019). Rapid transcrustal magma movement under Iceland. *Nature Geoscience*, 1.

Petrone, C. M., Bugatti, G., Braschi, E., & Tommasini, S. (2016). Pre-eruptive magmatic processes re-timed using a non-isothermal approach to magma chamber dynamics. *Nature communications*, *7*, 12946.

Pioli, L., Azzopardi, B. J., & Cashman, K. V. (2009). Controls on the explosivity of scoria cone eruptions: Magma segregation at conduit junctions. *Journal of Volcanology and Geothermal Research*, *186*(3-4), 407-415.

Putirka, K. D. (2008). Thermometers and barometers for volcanic systems. *Reviews in mineralogy and geochemistry*, *69*(1), 61-120.

Ruprecht, P., & Plank, T. (2013). Feeding andesitic eruptions with a high-speed connection from the mantle. *Nature*, *500*(7460), 68.

Ruscitto, D. M., Wallace, P. J., Johnson, E. R., Kent, A. J. R., & Bindeman, I. N. (2010). Volatile contents of mafic magmas from cinder cones in the Central Oregon High Cascades: Implications for magma formation and mantle conditions in a hot arc. *Earth and Planetary Science Letters*, *298*(1-2), 153-161.

Saunders, K., Blundy, J., Dohmen, R., & Cashman, K. (2012). Linking petrology and seismology at an active volcano. *Science*, *336*(6084), 1023-1027.

Syracuse, E. M., van Keken, P. E., & Abers, G. A. (2010). The global range of subduction zone thermal models. *Physics of the Earth and Planetary Interiors*, *183*(1-2), 73-90.

Till, C., Grove, T. L., Donnelly-Nolan, J. M., & Carlson, R. W. (2013, December). Depths and temperatures of mantle melt extraction in the southern Cascadia subduction zone. In *AGU Fall Meeting Abstracts*.

Till, C. B., Kent, A. J. R., Abers, G. A., Janiszewski, H. A., Gaherty, J. B., & Pitcher, B. W. (2019). The causes of spatiotemporal variations in erupted fluxes and compositions along a volcanic arc. *Nature communications*, *10*(1), 1-12.